Optical Society of America. Dongqing Cao, Partha P. Banerjee, and Ting-Chung Poon, "Image Edge Enhancement with Two Cascaded Acousto-Optic Cells with Contrapropagating Sound," Appl. Opt. 37, 3007-3014 (1998). doi: 10.1364/ao.37.003007

Image edge enhancement with two cascaded acousto-optic cells with contrapropagating sound

Dongqing Cao, Partha P. Banerjee, and Ting-Chung Poon

Basic real-time programmable image-processing operations are accomplished by use of acousto-optic (AO) cells. Instead of frequency-plane filters, the AO cells are placed directly behind the object. The one-dimensional edge-enhancement results with one AO cell can be improved by use of two AO cells that are placed in tandem with contrapropagating sound. The dominant second-derivative operation obtained from the transfer function of the undiffracted order works like a one-dimensional Laplacian operator that enables improved edge enhancement. © 1998 Optical Society of America

OCIS codes: 070.1060, 070.6760, 100.1160, 100.2980.

1. Introduction

Edge-detection techniques have been used widely in digital image processing such as image enhancement, image segmentation, shape matching, etc. In digital image processing edge detection can be realized in either the spatial or the spatial-frequency domain. The spatial-domain methods operate directly on the image pixels.[1] The first-derivative and second-derivative functions are two important methods of achieving edge detection in the spatial domain. The first-derivative operation can be represented as

$$|\nabla f(x, y)| = \left\{ \left[\frac{\partial f(x, y)}{\partial x} \right]^2 + \left[\frac{\partial f(x, y)}{\partial y} \right]^2 \right\}^{1/2}, \qquad (1)$$

and it is executed by various gradient operators, such as the Sobel mask (operator).[2]

First-derivative methods suffer from the disadvantage that they respond erratically on the ramp-intensity profile. The second-derivative methods overcome this problem because they can determine whether a pixel lies on the dark or the light side of an edge, and therefore edge detection is accomplished by determination of the locations of zero crossings.[3] The second-derivative function is often realized by the Laplacian operator:

$$\nabla^2 f(x, y) = \frac{\partial^2 f(x, y)}{\partial x^2} + \frac{\partial^2 f(x, y)}{\partial y^2}. \qquad (2)$$

Image processing in the spatial-frequency domain (k_x, k_y) is straightforward; it involves computing the Fourier transform of the image to be processed as $F(k_x, k_y) = \mathrm{F}\{f(x, y)\}$, multiplying $F(k_x, k_y)$ by a filter transfer function $H(k_x, k_y)$, and taking the inverse Fourier transform to produce the processed image $g(x, y) = \mathrm{F}^{-1}\{H(k_x, k_y)F(k_x, k_y)\}$. Because edges are associated with high-frequency components, edge detection can be realized in the spatial-frequency domain by a high-pass filtering process that reduces the low-frequency components of the original image.

Acousto-optic (AO) devices are based on the elasto-optic effect. The applied sound signal changes the refractive index of the AO medium, which generates a phase grating. The phase grating produces one (Bragg regime) or multiple (Raman–Nath regime) diffracted light beams.

AO devices play an important role in optical signal and image processing. AO modulator and deflector devices find a multitude of applications because they can impart the time-varying electrical information to light waves in real time.[4] The frequency-shifting property of the diffracted light is used in optical heterodyne applications that lead to the use of AO cells in image correlators.[5,6] AO cells were used by Mait *et al.*[7] in the Fourier plane as a dynamic spatial filter, resulting in morphological erosion and dilation operations. AO cells were also used by Balakshy[8] to broad-

D. Cao is with TeraStor Corporation, 95 West Plumeria Drive, San Jose, California 95134. P. Banerjee is with the Department of Electrical and Computer Engineering and Center for Applied Optics, University of Alabama at Huntsville, Huntsville, Alabama 35899. T.-C. Poon is with the Optical Image Processing Laboratory, Bradley Department of Electrical Engineering, Virginia Polytechnic Institute and State University, Blacksburg, Virginia 24061.

Received 10 June 1997; revised manuscript received 20 January 1998.

0003-6935/98/143007-08$15.00/0

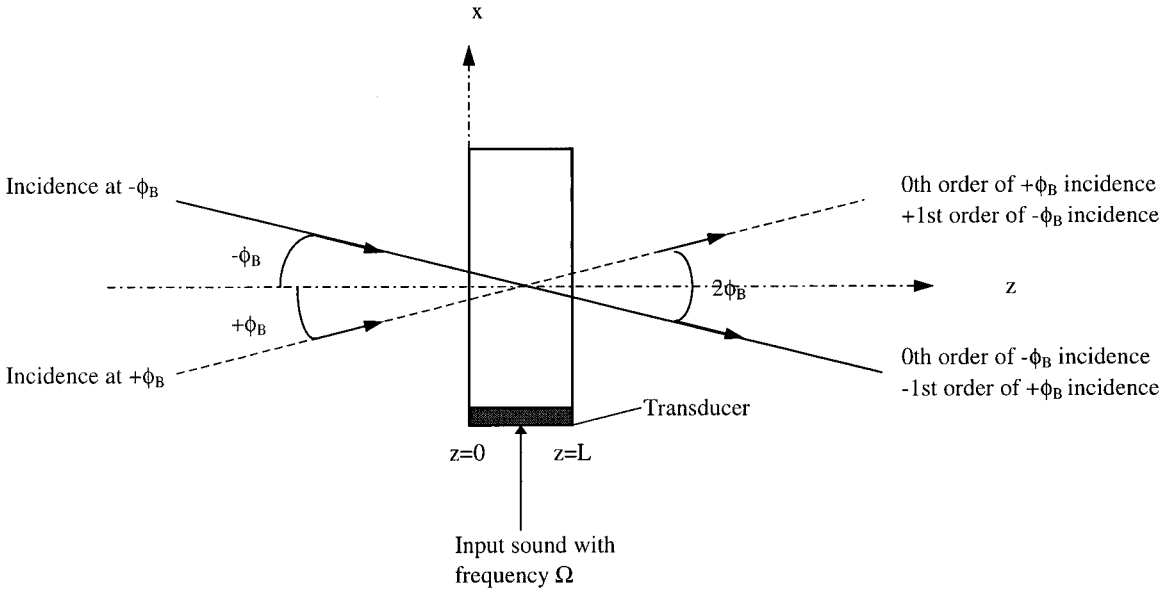

Fig. 1. Schematic diagram of AO diffraction at $\pm\phi_B$ incidences.

cast images into undiffracted and first diffracted orders.

More recently, image edge enhancement derived from high-pass spatial filtering in the image plane was achieved in the undiffracted order during Bragg diffraction by Banerjee *et al.*[9] and Xia *et al.*[10] Their approach was based on the selection of plane waves with chosen directions of propagation. Previous investigations based on this principle for spatial filtering include the study of Case[11]; however, in our case the spatial filtering occurs in real time and is programmable, since we use a dynamic electronically addressable grating in an AO device. In Ref. 11 it was reported that a fixed thick hologram in dichromated gel was used to demonstrate one-dimensional (1-D) differentiation. In this paper we also address the issue of asymmetric edge enhancement seen when one AO device is used. We observe and explain this effect as well as provide a means of alleviating this problem by using two AO cells with *contrapropagating* sound. By contrapropagating sound we mean that the two AO cells have traveling waves of (ultra)sound in opposing directions. The use of a Fabry–Perot etalon for image processing was investigated by Indebetouw.[12] Most recently the use of thick holograms for spatially filtering laser beams was demonstrated by Ludman *et al.*[13]

To explain the high-pass filtering characteristics of the undiffracted-order image physically, we can directly use the angular plane-wave spectrum concept. When a complex optical field is incident on an AO cell at the nominal Bragg angle, various spatial Fourier components corresponding to different spatial frequencies of the incident field can be identified as various plane waves traveling in different directions about the Bragg angle. The diffraction efficiency of the plane waves traveling nearer to the Bragg angle (corresponding to the lower spatial frequencies) is higher than that of the plane waves traveling at a larger deviation from the Bragg incidence angle (corresponding to the higher spatial frequencies). Hence the diffracted order shows low-pass characteristics, and the undiffracted order exhibits high-pass filtering as a result of energy conservation.

In this paper we theoretically as well as experimentally report the improvement of 1-D edge enhancement by using two AO cells in tandem with contrapropagating sound waves. In Section 2 a brief summary of 1-D edge enhancement by use of one AO cell is presented. Then improvements after using two AO cells are shown in Section 3. Section 4 concludes the paper.

2. Edge Enhancement with One Acousto-Optic Cell

As stated in Refs. 14–16, the interaction in an AO cell can be represented by its transfer functions in the spatial-frequency domain. When at Bragg incidence, $\phi_{\text{inc}} = \pm\phi_B$, and there are only the zeroth undiffracted order and minus–plus first diffracted orders, as shown in Fig. 1. The spatial transfer functions for the undiffracted orders in these two cases are derived as

$$H_0(k_x, z = L) = \exp\left[j\left(\frac{k_x^2 L}{2k_0} - \frac{k_x Q\Lambda_0}{4\pi}\right)\right] \times \left(\cos\left\{\left[\left(\frac{k_x Q\Lambda_0}{4\pi}\right)^2 + \left(\frac{\alpha}{2}\right)^2\right]^{1/2}\right\} \pm \left(\frac{jk_x Q\Lambda_0}{4\pi}\right)\frac{\sin\left\{\left[\left(\frac{k_x Q\Lambda_0}{4\pi}\right)^2 + \left(\frac{\alpha}{2}\right)^2\right]^{1/2}\right\}}{\left[\left(\frac{k_x Q\Lambda_0}{4\pi}\right)^2 + \left(\frac{\alpha}{2}\right)^2\right]^{1/2}}\right), \quad (3)$$

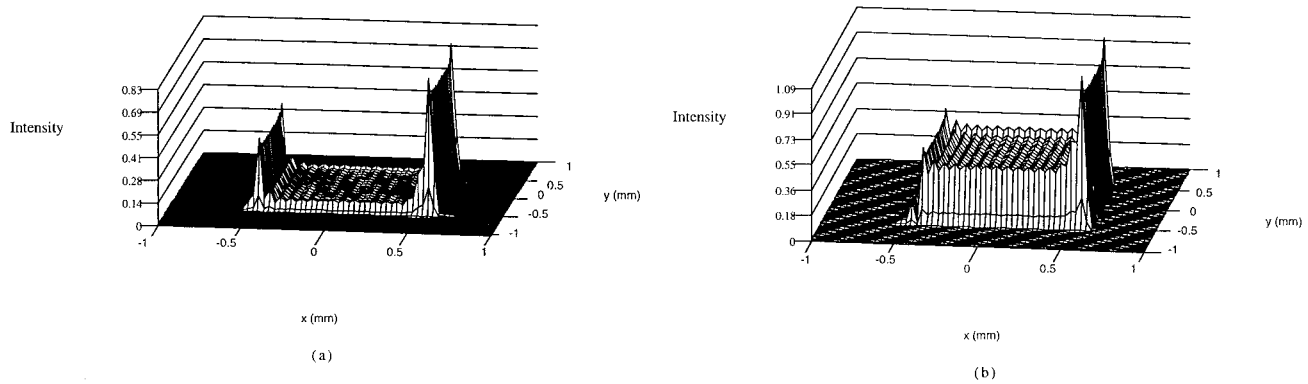

Fig. 2. Numerical simulation results demonstrated in three-dimensional (3-D) intensity-distribution format by use of one AO cell. The square input object has 1-mm sides, unit intensity, and $Q \approx 28$: (a) Asymmetric edges visible at $\alpha = 0.85\pi$. (b) For $\alpha = 0.6\pi$, one of the two vertical edges can hardly be distinguished.

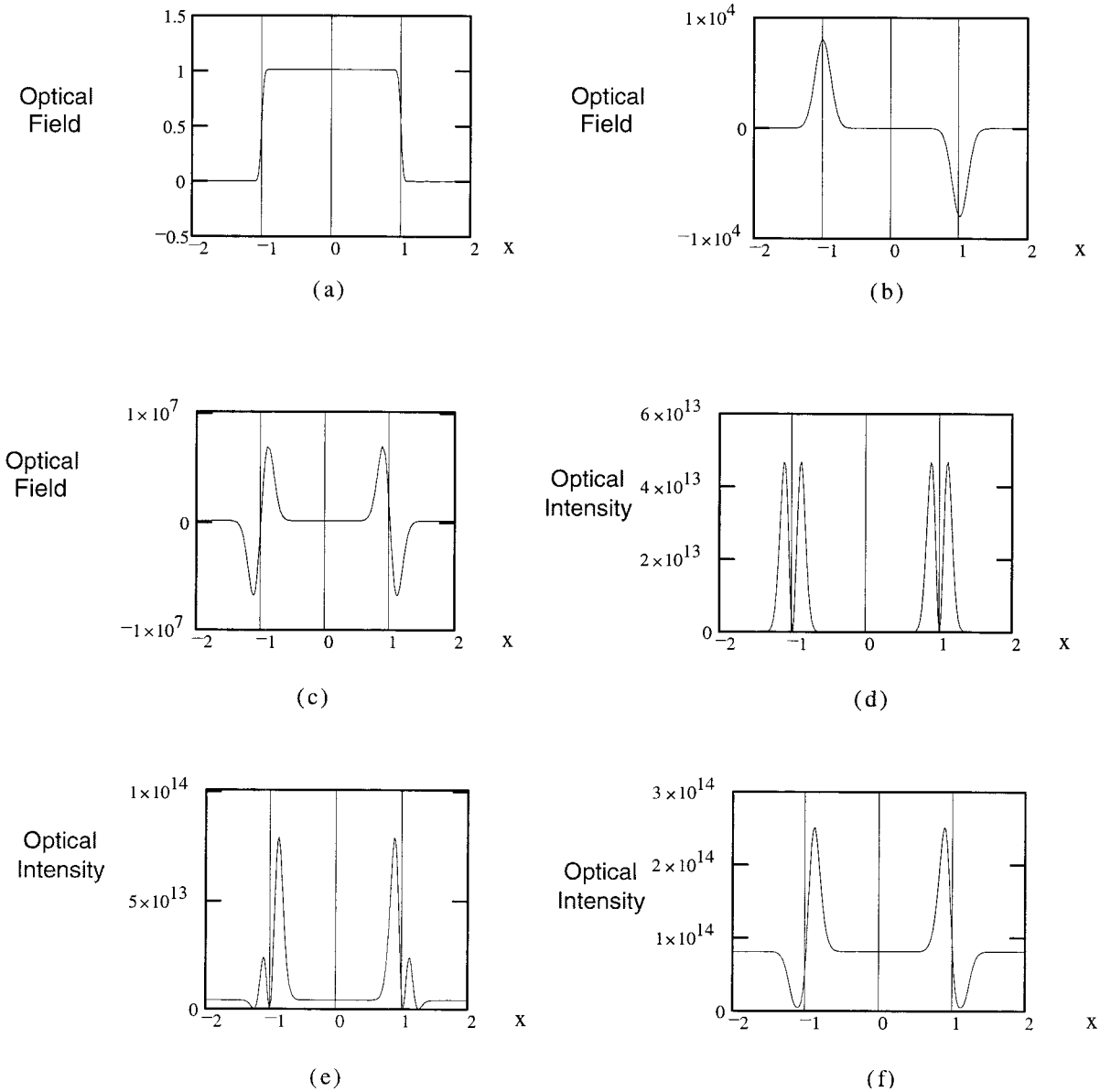

Fig. 3. Schematic diagrams illustrating the second-derivative effect: (a) Square input object field distribution. (b) Optical field after the first derivative with a zero constant term. (c) Optical field after the second derivative with a zero constant term. (d) Optical intensity after the second derivative with a zero constant term showing the well-defined double peaks near each edge. (e) Optical intensity after the second derivative but with a small nonzero constant. (f) Optical intensity after the second derivative but with a large nonzero constant.

where the plus sign between the cosine and sine terms applies to the case of $\phi_{inc} = +\phi_B$ and the minus sign applies to $\phi_{inc} = -\phi_B$, $Q = (2\pi\lambda L)/\Lambda_0^2$ is the Klein–Cook parameter, α represents the peak phase delay and is proportional to the sound pressure, L is the interaction length, Λ_0 is the sound wavelength, λ is the light wavelength in the AO medium, k_0 denotes the propagation constant of light in the AO medium, and k_x denotes the spatial frequency of the diffracted light along the transverse (x) direction. The propagational diffraction effect through the length of the AO cell is represented by the phase term $\exp[j(k_x^2 L/2k_0)]$. The second part of the phase-term exponential in Eq. (3) (the linear term in k_x) gives rise to a shift in the position of the pattern in the far field. The remaining terms in Eq. (3) characterize the AO interaction process. Equation (3) therefore shows that, in essence, the propagational diffraction effects are *decoupled* from the AO interaction process.

The numerical calculations of the spatial transfer functions are performed with the computer. We have published the details in Ref. 9. The results show that, under certain conditions, the transfer function for the undiffracted order exhibits high-pass filtering properties and the transfer function for the first diffracted order exhibits low-pass filtering characteristics. Also, these high- and low-pass filtering characteristics are programmable in real time by variation of the peak phase delay α. Under our experimental conditions of a Klein–Cook parameter of $Q \approx 28$, the values of α are restricted to the range of less than π, and when $\alpha > 0.6\pi$ the undiffracted-order transfer function exhibits high-pass (edge-enhancement) filtering characteristics.

We can explain the phenomenon of high-pass spatial filtering theoretically from the transfer function as shown in Eq. (3). As mentioned above, the first exponential term in Eq. (3) is the propagational diffraction term. One can exclude it by properly setting the experiment up, as stated below. The second exponential term in Eq. (3) is related to the spatial position shift and is inconsequential to the analysis, regardless of whether it is included. Under our experimental conditions, $|(k_{x\max} Q\Lambda_0)/4\pi| \ll |\alpha/2|$; therefore the undiffracted-order transfer function can be expressed as

$$H_0(k_x) \approx A \pm jBk_x, \tag{4}$$

where the plus sign represents the case of $\phi_{inc} = +\phi_B$ and the minus sign represents the case of $\phi_{inc} = -\phi_B$, $A \approx \cos(\alpha/2)$, and $B \approx (\phi\Lambda_0/4\pi)\{[\sin(\alpha/2)]/(\alpha/2)\}$. From the Fourier transform property we have $F_x\{[\partial f(x,y)]/\partial x\} = -jk_x F_x\{f(x,y)\}$, so the amplitude of the undiffracted order E_0 after the AO cell can be written approximately as

$$E_0(x,y) = \left(A \mp B\frac{\partial}{\partial x}\right)E_{inc}(x,y), \tag{5}$$

where $E_{inc}(x,y)$ is the optical field incident on the AO cell. The signs in Eqs. (5) are consistent with those in expressions (4). Experimentally it is noted that, for the objects used and when α is near π, the second part of the right-hand side (RHS) of Eqs. (5) is dominant. We point out that our approximated expressions (4) are different from the corresponding expression in Ref. 11 because of the regime of α that we use in our experiment. Therefore the effect of the AO cell on the undiffracted order is just like edge enhancement by a 1-D gradient operator in digital image processing, as explained above. However, unlike digital image processing, this edge enhancement takes place in real time and the amount of enhancement is programmable, since the α of the AO cell can easily be changed by variation of the sound pressure.

3. Improvement of Edge Enhancement with Two Acousto-Optic Cells

A. Theoretical Analysis

It is found from our experimental results and numerical simulations that edge enhancement with one AO cell is not symmetric, i.e., with a square input object the intensities of the square's two vertical edges, for instance, are not equal. The numerical simulations for $\alpha = 0.85\pi$ and $\alpha = 0.6\pi$ are shown in Figs. 2(a) and 2(b), respectively, for a square object with sides of 1 mm. The numerical simulations show that the asymmetry is an effect of the first term on the RHS in Eqs. (5) that cannot be ignored completely. In our previous paper[9] only the brightness profile of the edges was shown, and the asymmetry did not appear in the numerical simulations because the magnitude of the transfer function was used. To reduce this asymmetry we used two AO cells that are placed in tandem with contrapropagating sound waves. If an object is incident on the first AO cell at $+\phi_B$, the undiffracted beam after the first AO cell is then incident on the second AO cell at $-\phi_B$ because of the contrapropagating sound wave. Then from Eqs. (5) and Fig. 1 the complex optical field of the undiffracted order after the first AO cell can be approximated as

$$E_0^{(1)}(x,y) = \left(A_1 - B_1\frac{\partial}{\partial x}\right)E_{inc}(x,y), \tag{6}$$

and the undiffracted optical field after the second AO cell can be expressed approximately as

$$E_0^{(2)}(x,y) = \left(A_2 + B_2\frac{\partial}{\partial x}\right)E_0^{(1)}(x,y), \tag{7}$$

where A_1, A_2 and B_1, B_2 are the same functions as A and B, respectively, but the terms α, Q, and Λ_0 in the relations for A and B are the parameters of the first and second AO cells, respectively. From Eqs. (6) and (7) the undiffracted optical field after the two AO cells can be written as

$$E_0^{(2)}(x,y) = \left(A_1A_2 + A_1B_2\frac{\partial}{\partial x} - A_2B_1\frac{\partial}{\partial x} - B_1B_2\frac{\partial^2}{\partial x^2}\right)E_{inc}(x,y). \tag{8}$$

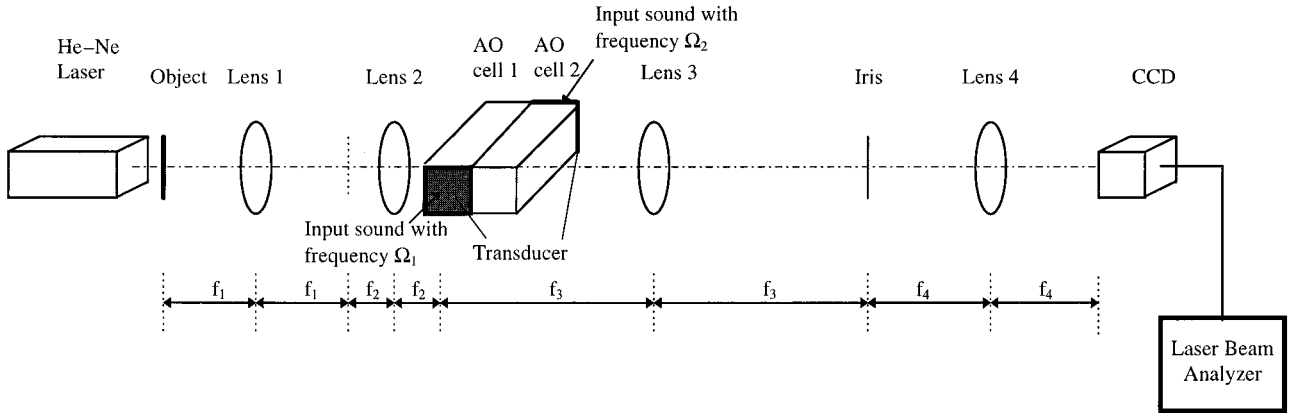

Fig. 4. Experimental setup for 1-D edge enhancement by use of two cascaded AO cells with contrapropagating sound.

When the parameters of the two AO cells are the same, $A_1 = A_2$ and $B_1 = B_2$; therefore $A_1B_2 = A_2B_1$, and the second and third terms in parentheses on the RHS of Eq. (8), which contains the first-order derivative terms, are canceled. If both AO cells' peak phase-delay parameters α_1 and α_2 are near π (i.e., $\alpha_1 = \alpha_2 \approx 0.85\pi$), the term A_1A_2 is small; therefore the second-order derivative term is dominant and works as a 1-D Laplacian operator.

Edge detection can be accomplished by determination of the locations of the zero crossings of the double peaks on both sides of the edges. Furthermore, the undiffracted-order beam profile can be programmed by the value of the constant term, which varies with the sound intensity of both AO cells. This phenomenon can be explained by use of the 1-D schematic diagrams shown in Fig. 3. With a zero constant term and for a square object, as shown in Fig. 3(a), the optical field after the first derivative can be approximated as shown in Fig. 3(b). The optical field responsible for the second-derivative operation [see the last term on the RHS in Eq. (8)] is shown in Fig. 3(c). The zero crossing between the double peaks near the edges appears in the intensity profile [see Fig. 3(d)], and edge detection is performed by determination of the location of the zero crossing between the double peaks.

Unfortunately, the A_1A_2 term in Eq. (8) cannot always be equal to zero in practice. To simulate the effect of the nonzero constant term, we add various positive values of the constant to the last term in Eq. (8). Figures 3(e) and 3(f) show two examples of the intensity profiles with two different values of the constant. For a range of values we see that the well-defined double peaks are deformed. As the value of the constant increases from zero to the maximum peak value of the optical field profile in Fig. 3(c), the outer peaks in the intensity profile, which indicate the dark side of each edge (see paragraph two in Section 1), become increasingly lower, and two zeros appear near each edge [Fig. 3(e)]. If the value of the constant exceeds the maximum peak value of the field shown in Fig. 3(c), the outer peaks disappear and valleys appear instead [Fig. 3(f)]. If the value of the constant is small compared with the maximum peak value of the field shown in Fig. 3(c), the edges can still be identified by determination of the location of the zero crossing between the double peaks near each edge [see, e.g., Fig. 3(e)]. However, when the constant term is near to or larger than the maximum peak value [e.g., Fig. 3(f)], only the symmetric inner peaks are evident, and they actually show the light side of each edge (see paragraph two in Section 1). Therefore we can realize edge detection by locating the brighter side of each edge.

B. Experimental Results

The experimental setup is shown in Fig. 4. A He–Ne laser ($\lambda = 633$ nm) is the light source. A square transparency with 2-mm sides is used as the object. Lenses 1 and 2 are used to decrease the effective object size by a factor of 2. The first AO cell is placed immediately behind the image plane of the lens 1, 2 combination. It is an IntraAction Model AOM-40 with a carrier frequency of 40 MHz. The AO interaction length is approximately 62.5 mm. The AO medium is flint glass with a refractive index of 1.68, and the sound velocity in the material is approximately 3.96 km/s.

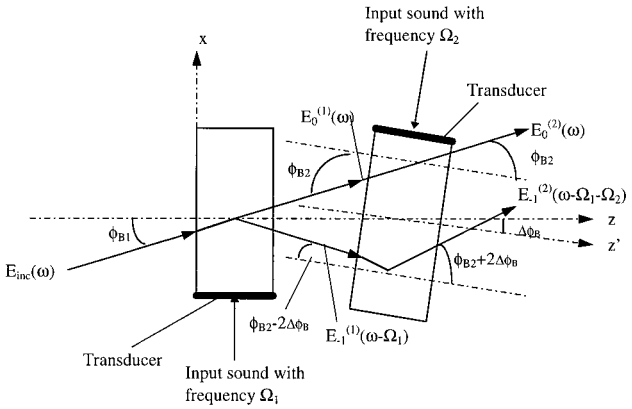

Fig. 5. Schematic diagram showing how to overcome overlap diffraction from slightly different sound frequencies for the two cascaded AO cells: $\phi_{B1} = \lambda/2\Lambda_1$, $\phi_{B2} = \lambda/2\Lambda_2$, and $\Delta\phi_B = \phi_{B_2} - \phi_{B_1}$.

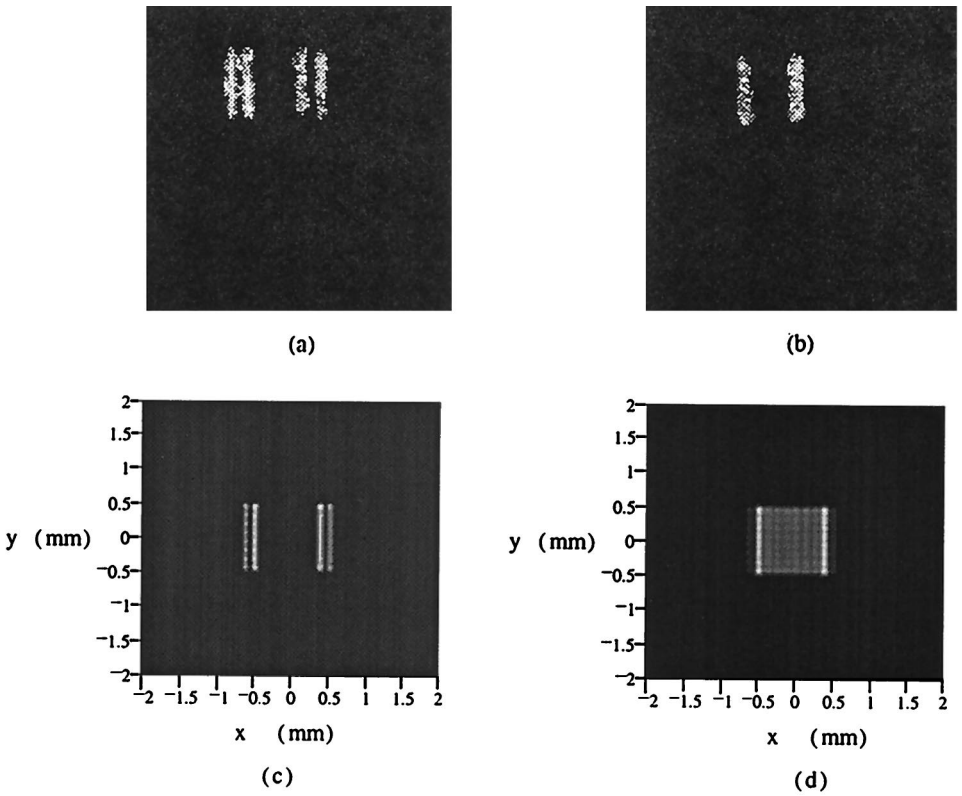

Fig. 6. Experimental and numerical simulation results from two cascaded AO cells. The incident object is a square with sides of 2 mm that are demagnified to 1 mm. (a) Experimental result of edge detection by the location of the zero crossing with $\alpha_1 = \alpha_2 \approx 0.85\pi$. (b) Experimental result showing the two symmetric light-side edges with $\alpha_1 = \alpha_2 \approx 0.6\pi$. (c) Numerical simulation result demonstrated by the brightness profile with $\alpha_1 = \alpha_2 \approx 0.85\pi$; it matches the results shown in (a) well. (d) Numerical simulation result demonstrated by the brightness profile with $\alpha_1 = \alpha_2 \approx 0.6\pi$; it matches the results shown in (b) well.

The second AO cell is similar to the first but with a contrapropagating sound wave. The iris in the back focal plane of lens 3 is used to select the undiffracted order for display. Lenses 3 and 4 are used to image the object exactly on the CCD detector array of a Spiricon laser beam analyzer; two convex lenses with focal lengths of 150 and 100 mm are used for lens 3 and lens 4, respectively. Therefore the propagational diffraction effect between the AO cell and the CCD camera (which, as explained in Section 2, includes diffraction through the AO cell but is decoupled from the interaction process) has been taken into account.

The sound frequencies of the two AO cells are selected to be slightly different to overcome overlap diffraction, which is described in detail below. The sound frequencies of the first and the second AO cells are approximately 55 and 68 MHz, respectively. Because the two AO cells have different sound frequencies Ω_1 and Ω_2 (corresponding to wavelengths Λ_1 and Λ_2, respectively), the Bragg angles of the two cells (ϕ_{B_1} and ϕ_{B_2}) are different too. To allow the undiffracted order after the first AO cell $E_0^{(1)}$ to be incident on the second cell at an angle of ϕ_{B_2}, we need to rotate the z axis of the second AO cell by $\Delta\phi_B$ ($\Delta\phi_B = \phi_{B_2} - \phi_{B_1}$) to z', as shown in Fig. 5. Therefore the diffracted order $E_{-1}^{(1)}$ after the first AO cell is incident on the second cell at an angle of ($\phi_{B_2} - 2\Delta\phi_B$), and its diffracted order $E_{-1}^{(2)}$ after the second cell propagates in the direction shown in Fig. 5. As is clear from Fig. 5, the orders $E_0^{(2)}$ and $E_{-1}^{(2)}$ propagate in different directions. Note that, if the two AO cells have the same sound frequency, $\Delta\phi_B$ will be equal to zero. From Fig. 5 we can see that in this case $E_0^{(2)}$ and $E_{-1}^{(2)}$ will propagate in the same direction and have different frequencies, which complicates analysis and detection and thus was not considered in the above theory.

The experimental results showing the edge location at the zero crossing of the double peaks at $\alpha_1 = \alpha_2 \approx 0.85\pi$ are shown in Fig. 6(a). For $\alpha_1 = \alpha_2 \approx 0.6\pi$, the zero crossings of well-defined double peaks are no longer visible [Fig. 6(b)], but the symmetric bright side of each vertical edge is evident. The results agree well with the theoretical explanation advanced in Subsection 3.A and with the numerical simulations based on theory, as shown in Figs. 6(c) and 6(d). More on the numerical simulations follows in Subsection 3.C. The corresponding experimental results at $\alpha \approx 0.85\pi$ and $\alpha \approx 0.6\pi$ for one AO cell are shown in Figs. 7(a) and 7(b), respectively. We can see that, at higher values of α, the intensities of the two edges shown in Fig. 7(a) are not the same and that at lower values of α one of the two vertical edges can hardly be distinguished. Therefore the

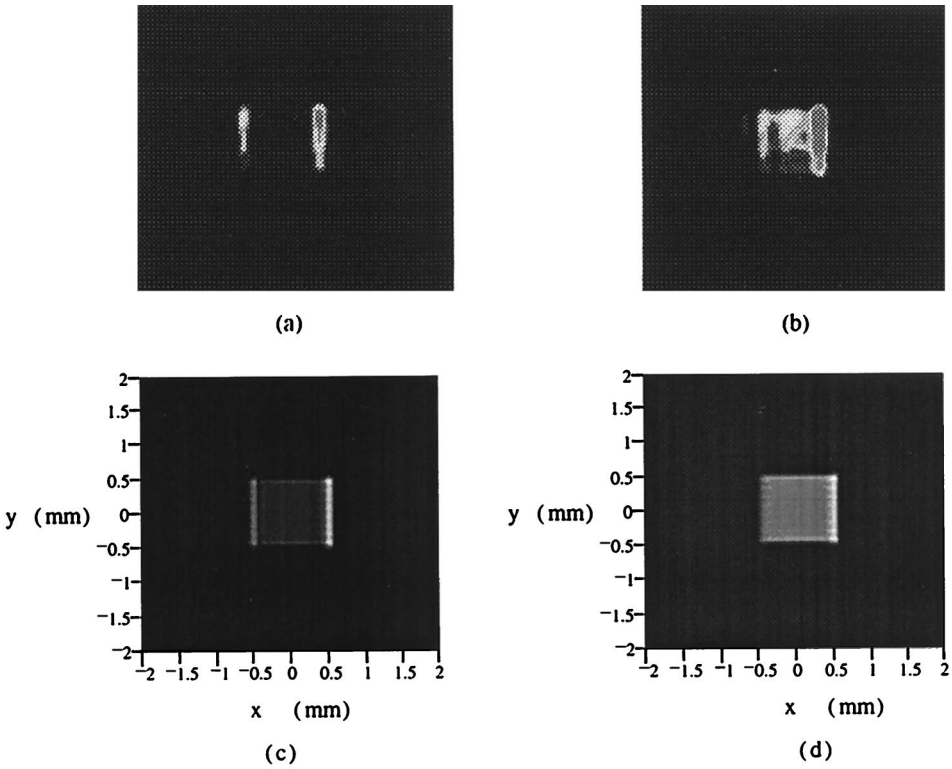

Fig. 7. Experimental and numerical simulation results from one AO cell. The incident object is a square with 2-mm sides that are demagnified to 1 mm. (a) Experimental result of two asymmetric edges at $\alpha \approx 0.85\pi$. (b) Experimental result at $\alpha \approx 0.6\pi$; one of the two vertical edges can hardly be distinguished. (c) Numerical simulation result demonstrated by the brightness profile at $\alpha \approx 0.85\pi$. (d) Numerical simulation result demonstrated by the brightness profile at $\alpha \approx 0.6\pi$.

edge-enhancement results are improved greatly by use of two AO cells.

C. Note on the Numerical Simulations

On the basis of the experimental conditions described in paragraph one of Subsection 3.B, the Klein–Cook parameter Q is approximately 28. A discrete Fourier transform method is used to simulate the experiment. The undiffracted-order transfer function for Bragg incidence is multiplied by the angular plane-wave spectrum of the square input object to derive the spectrum of the processed image at the exit of the AO cell. The inverse Fourier transform of the exit spectrum is equivalent in shape to the field pattern at the CCD detector (which is placed at the back focal plane of lens 4).

For $\alpha_1 = \alpha_2 \approx 0.85\pi$ and $\alpha_1 = \alpha_2 \approx 0.6\pi$, the results of numerical simulation of the brightness profile for a two-AO-cell implementation of 1-D edge enhancement are shown in Figs. 6(c) and 6(d). The corresponding numerical simulations for a one-AO-cell implementation are shown in Figs. 7(c) and 7(d), cor-

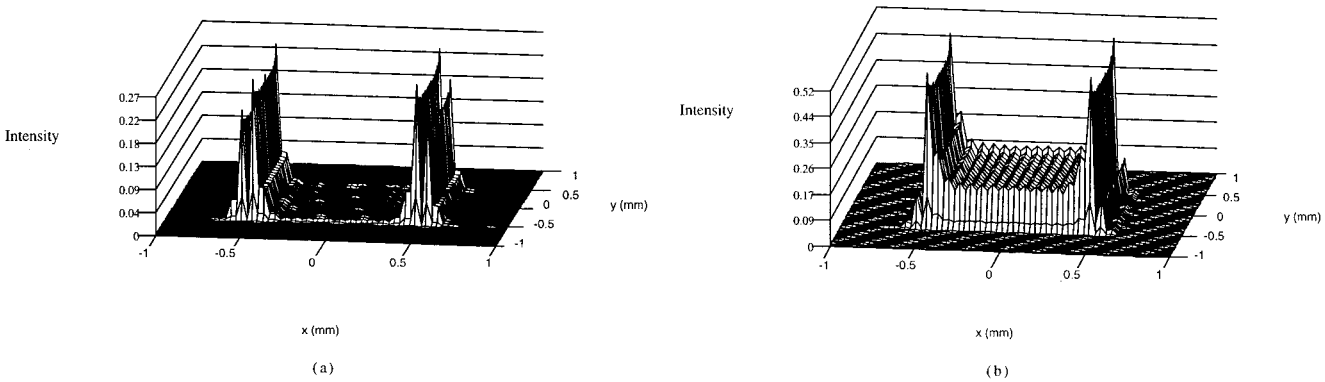

Fig. 8. Numerical simulation results demonstrated in 3-D intensity-distribution format by use of two cascaded AO cells. The square input object has 1-mm sides, unit intensity, and $Q \approx 28$. (a) Edge location at the zero crossing between double peaks near each edge at $\alpha_1 = \alpha_2 \approx 0.85\pi$. (b) Two symmetric light-side two vertical edges evident at $\alpha_1 = \alpha_2 \approx 0.6\pi$.

responding to the experimental results shown in Figs. 7(a) and 7(b), respectively. Figures 6(a) and 6(c) show edge detection by means of locating the zero crossings of the double peaks. The corresponding 3-D intensity distribution is shown in Fig. 8(a). Also, Figs. 6(b) and 6(d) show the two symmetric light-side vertical edges of the square input object, and the corresponding 3-D intensity distribution is shown in Fig. 8(b). After comparing Figs. 8(a) and 8(b) with Figs. 2(a) and 2(b), we can see that the asymmetry has almost disappeared and symmetric edge enhancement can be obtained at a lower peak phase delay α by use of two AO cells.

4. Conclusions

A novel, to our knowledge, programmable optical image-processing technique with two AO cells has been introduced. Two AO cells that are placed in tandem with contrapropagating sound at slightly different frequencies are used to improve the results obtained with only one AO cell. Numerical simulations have verified the experimental results. Extension of this technique to two-dimensional image processing is possible by use of four AO cells.

References

1. R. C. Gonzalez and R. E. Woods, *Digital Image Processing* (Addison-Wesley, New York, 1993).
2. M. A. Stedham, "Spacecraft attitude determination via the panoramic annular lens attitude determination system (PALADS)," Masters thesis (University of Alabama in Huntsville, Huntsville, Al., 1994).
3. T. Y. Young and K.-S. Fu, *Handbook of Pattern Recognition and Image Processing* (Academic, New York, 1986).
4. P. Das, *Acousto-optic Signal Processing: Fundamentals and Applications* (Artech House, Norwood, Mass., 1991).
5. R. Whitman, A. Korpel, and S. Lotsoff, "Application of acoustic Bragg diffraction to optical processing techniques," in *Proceedings of the Symposium on Modern Optics* (Wiley, New York, 1967), pp. 243–246.
6. M. King, W. R. Bennett, L. B. Lambert, and M. Arm, "Real-time electrooptical signal processors with coherent detection," Appl. Opt. **6,** 1367–1375 (1967).
7. J. N. Mait, D. W. Prather, and R. A. Athale, "Acousto-optic processing with electronic feedback for morphological filtering," Appl. Opt. **31,** 5688–5699 (1992).
8. V. I. Balakshy, "Scanning of images," Sov. J. Quantum Electron. **6,** 965–971 (1979).
9. P. P. Banerjee, D. Cao, and T.-C. Poon, "Basic image-processing operations by use of acousto-optics," Appl. Opt. **36,** 3086–3089 (1997).
10. J. Xia, D. B. Dunn, T.-C. Poon, and P. P. Banerjee, "Image edge enhancement by Bragg diffraction," Opt. Commun. **128,** 1–7 (1996).
11. S. Case, "Fourier processing in the object plane," Opt. Lett. **4,** 286–288 (1979).
12. G. Indebetouw, "Tunable spatial filtering with a Fabry-Perot etalon," Appl. Opt. **19,** 761–764 (1980).
13. J. E. Ludman, J. R. Riccobona, N. O. Reinhand, I. V. Semenova, Y. L. Korzinin, S. M. Shahviar, H. J. Caulfield, J. M. Fournier, and P. Hemmer, "Very thick holographic nonspatial filtering of laser beams," Opt. Eng. **36,** 1700–1705 (1997).
14. M. R. Chatterjee, T.-C. Poon, and D. N. Sitter, Jr., "Transfer function formalism for strong acousto-optic Bragg diffraction of light beams with arbitrary profiles," Acustica **71,** 81–92 (1990).
15. A. Korpel, P. P. Banerjee, and C.-W. Tarn, "A unified treatment of spectral formalisms of light propagation and their application to acousto-optics," Opt. Commun. **97,** 250–258 (1993).
16. P. P. Banerjee and C.-W. Tarn, "A Fourier transform approach to acousto-optic interactions in the presence of propagational diffraction," Acustica **74,** 181–191 (1991).